Lattice Dynamics and Electron-Phonon-Coupling Field and Vibronic Spectra*

D. H. Kühner,† H. V. Lauer,‡ and W. E. Bron
Department of Physics, Indiana University, Bloomington, Indiana 47401
(Received 5 November 1971)

Details of the dynamical properties of crystalline lattices are tested against vibronic spectra accompanying electronic transitions of Sm^{2+} probe ions. Dispersion relations and shell-model parameters are presented for CaF_2, $SrCl_2$, and EuF_2. Considerable information is also obtained on the symmetry and nature of the electron-phonon-coupling field. It is shown that long-range Coulombic and highly local, non-Coulombic fields are involved. Furthermore, it is indicated that previously reported deficiencies in shell models concerning the prediction of the dielectric constant and the dynamical polarization have a probable origin in the neglect of extended, partially overlapping, electronic distributions.

I. INTRODUCTION

The authors and their co-workers have shown in a series of papers[1-10] that the lattice dynamics of some insulator crystals can be independently tested against vibronic spectra (see also Refs. 11 and 12). Vibronic spectra form a particularly critical basis for models of lattice dynamics, since such spectra not only contain information on eigenvalues, but also contain information on eigenvectors.

In a preceding work by Kühner[10] the technique has been applied to the SrF_2 and BaF_2 lattices. It is shown that vibronic spectra can be theoretically reproduced in terms of the ideal dynamics of each lattice as described by a shell model. The parameters of the model are fitted, with one exception, to independently obtained macroscopic data. The exception involves a decrease of roughly 20% in the experimentally obtained high-frequency dielectric constant.[10] This change is required in order to bring the energy, at which various features of the calculated vibronic spectra occur, into coincidence with those obtained experimentally. It was further noted that the shell models lead to an apparent overestimation of the dynamical polarization. This effect has also been noticed in similar work carried out on alkali halide lattices.[6]

The calculations of the alkaline-earth fluoride lattices mentioned above, and the earlier ones on alkali halide lattices,[6,7,11,12] are, however, complicated by the possibility that the observed discrepancies stem from distortions in the lattice which result from the presence of the optically active probe ion. In these studies, vibronic spectra accompanying intraconfigurational optical transitions of the Sm^{2+} ion have been used. In order to eliminate possible distortional effects, we have investigated in detail the system $EuF_2:Sm^{2+}$. As is the case throughout the alkaline-earth halides, the Sm^{2+} ion replaces substitutionally the cation: in this case the Eu^{2+} ion. These two ions differ only by one $4f$ electron, by 1.3% in atomic weight, and have essentially identical ionic radii and outer electron shell.

In order to study further the possible overestimation by the shell models of the electronic polarizability, we have also investigated the system $SrCl_2:Sm^{2+}$. Since chlorine ions are more polarizable than fluoride ions, the discrepancy between calculated and experimental vibronic spectra is predicted to be more pronounced in the $SrCl_2$ case.

Finally, in order to show that the technique works equally well for vibronic spectra accompanying interconfiguration (rather than intraconfiguration) transitions, we have also investigated the $CaF_2:Sm^{2+}$ system.

We show that not only the details of the dynamics of these lattices can be successfully tested against the vibronic spectra, but that in addition vibronic spectra lead to information on the nature of the electron-phonon-coupling field. Furthermore, we show that the discrepancies in the calculated high-frequency dielectric constant noted above may originate from the use of point-multipole charge distributions rather than extended, partially overlapping, electronic charge distributions, in the description of the electron-phonon coupling.

II. EXPERIMENTAL METHODS

Single crystals of $SrCl_2$, containing Sm^{3+}, were grown in an induction furnace by the Czochralski method, and then annealed at 700 °C for 12 h to relieve strains. EuF_2 crystals, containing Sm^{2+}, were grown from EuF_3 powder (containing SmF_3) by melting in a vitreous carbon crucible at 1450 °C under a pure-hydrogen atmosphere.[13] In this method, EuF_2 crystals slowly freeze out from the melt via the reaction $2EuF_3 + H_2 \rightarrow 2EuF_2 + 2HF$. Crystals of CaF_2, containing Sm^{3+}, were purchased from Optovac Inc.[14] The nominal samarium con-

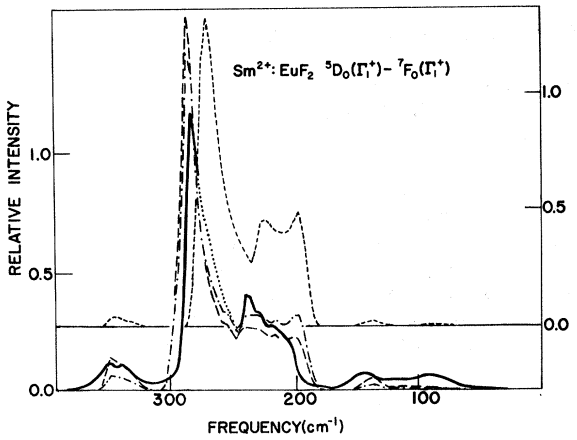

FIG. 1. Curve (a) (solid line) is the measured sideband of the $^5D_0(\Gamma_1^+) \rightarrow {}^7F_0(\Gamma_1^+)$ transition of $EuF_2 : Sm^{2+}$. The overlap region with the $^5D_0(\Gamma_1^+) \rightarrow {}^7F_1(\Gamma_1^+)$ zero-phonon line is shown by the dotted line. Curve (b) (dashed line) is the dipolar sideband calculated with the SDM. Curve (c) (dot-dashed line) is the rigid-ion-coupling case. Curve (d) (dashed line), which is shifted up in scale, is the calculated sideband on the basis of an ASM, where $\epsilon_\infty^{\text{theor}} = \epsilon_\infty^{\text{expt}}$. Note that frequency increases to the left on all such graphs.

tent in each case was 0.05 mole%. The Sm^{3+} in $SrCl_2$, and in CaF_2, was reduced to Sm^{2+} by heating in a three-zone furnace to near the melting point under the corresponding alkaline-earth-metal vapor.

Optical emission spectra were taken using a 1-m Jarrell-Ash Czerny-Turner spectrometer set to a resolution of 2 Å in the region of the relatively intense zero-phonon lines. Zeeman studies were carried out using a superconducting coil capable of 100-kG fields with a homogeneity of 5 parts in 10^5 over the entire sample. The coil and samples were immersed in liquid helium at 4.2 °K. Polarization measurements were taken of the emitted light in a direction perpendicular to the magnetic field axis. Unfortunately, polarization measurements of light emitted parallel to the magnetic field were inconclusive because of stray light problems in the experimental apparatus.

III. EXPERIMENTAL RESULTS

Emission and Zeeman spectra have been recorded for the following four transitions of Sm^{2+} in EuF_2 and $SrCl_2$:

$$^5D_0(\Gamma_1^+) \rightarrow {}^7F_0(\Gamma_1^+)\,, \quad {}^5D_0(\Gamma_1^+) \rightarrow {}^7F_1(\Gamma_4^+)\,,$$

$$^5D_0(\Gamma_1^+) \rightarrow {}^7F_2(\Gamma_3^+)\,, \quad {}^7F_2(\Gamma_5^+)\,.$$

Here the group-theoretic term assignments for the electronic states follow those of the Sm^{2+} ion in other alkaline-earth halide lattices, i.e., SrF_2 and BaF_2.[15] In addition, the sideband structure of the transition corollary to the $^5D_0 \rightarrow {}^7F_0$ transition of the Sm^{2+} in CaF_2 has also been recorded. This transition has been shown[15] to originate from a state belonging to the $4f^5\,5d$ configuration, rather than from the $^5D_0$ state which belongs to the $4f^6$ configuration.

The vibronic spectra measured in zero magnetic field at 4.2 °K are shown in Figs. 1–5.

A problem exists in assigning frequencies to the vibronic sideband with respect to the pure electronic transition in the $EuF_2 : Sm^{2+}$ and $SmCl_2 : Sm^{2+}$ cases. Only the $^5D_0 \rightarrow {}^7F_1$ transition is an allowed magnetic dipole transition, whereas the other transitions are neither electric dipole nor magnetic dipole allowed. A "zero-phonon" line is, therefore, only observed for the $^5D_0 \rightarrow {}^7F_1$ transition. It should, however, be noted from the top three graphs of Figs. 2 and 4 that the maximum B is a dominant feature of each of the vibronic sidebands. It will be shown in Sec. V that this

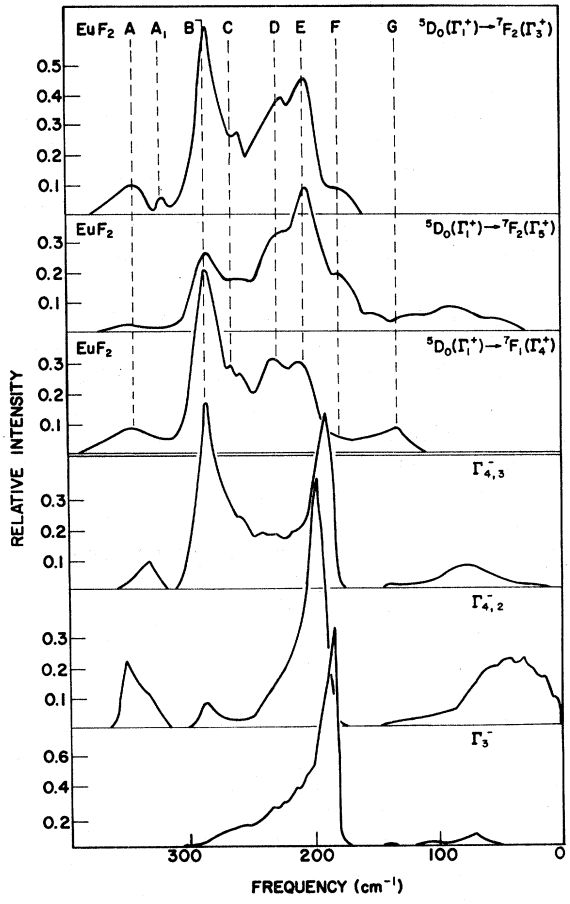

FIG. 2. The upper three curves are the measured sidebands of the $^5D_0(\Gamma_1^+) \rightarrow {}^7F_1(\Gamma_4^+)$, $^7F_2(\Gamma_4^+)$, $^7F_2(\Gamma_3^+)$ transitions of Sm^{2+} in EuF_2. The lower curves are sidebands calculated with the SDM.

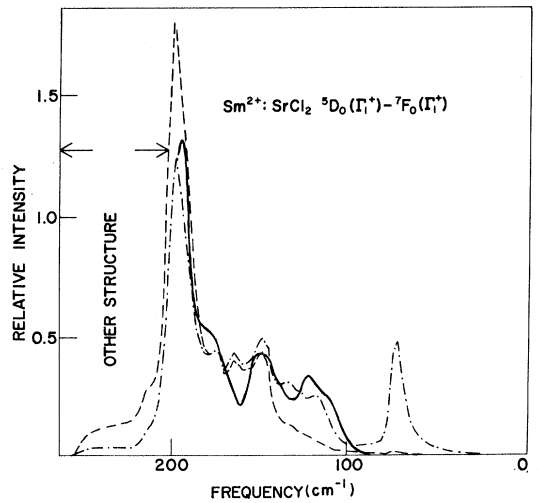

FIG. 3. Curve (a) (solid line) is the experimental sideband of the $^5D_0(\Gamma_1^+) \rightarrow {}^7F_0(\Gamma_1^+)$ transition of $Sm^{2+}:SrCl_2$. Curve (b) (dot-dashed line) is the dipolar sideband calculated with the ASM. Curve (c) (dashed line) is the rigid-ion-coupling case. The region of the unknown additional structure is indicated in the graph.

maximum always occurs at the same frequency in the directly calculated sidebands. We have, accordingly, adopted the relative frequency of this maximum with the zero-phonon line of the $^5D_0 \rightarrow {}^7F_1$ transition as a gauge with which to determine the frequencies of the other sidebands. This procedure yields a consistent assignment in the $EuF_2:Sm^{2+}$ system. It is also in agreement with the frequency assignments given by Cohen and Guggenheim[16] for the $SrF_2:Sm^{2+}$ systems.

A slight problem arises in the frequency assignment for the $SrCl_2:Sm^{2+}$ system. The $^5D_0 \rightarrow {}^7F_0$ sideband of $SrCl_2$ has unexplained structure in the region of the longitudinal-optical limiting frequency. This structure is also evident in the sidebands published for this system by Axe and Sorokin.[17] The fact that the structure is not observed in the sidebands of other transitions leads us to suspect that it does not result from any lattice vibrations. If this structure is ignored, a consistent frequency assignment can again be made based on a dominant peak in the $^5D_0 \rightarrow {}^7F_1$ sideband, i.e., in a manner similar to that described above for the $EuF_2:Sm^{2+}$ system.

Application of a magnetic field in the [100] direction of the fluorite lattice lowers the site symmetry of the Sm^{2+} ion from O_h to C_{4h}. With fields of the order of 90 kG, we find easily observable splittings of 6 to 10 cm^{-1} in the zero-phonon lines of the $^5D_0(\Gamma_1^+) \rightarrow {}^7F_1(\Gamma_4^+)$ transition. The Zeeman components of the vibronic sidebands, on the other hand, cannot be resolved, since the splitting is of the same order as the width of the main phonon peaks. Nevertheless, a net polarization of the various features of the sideband is observed.

Actually, the inability, in the present measurements, to determine the polarization of the emitted light parallel to the direction of the magnetic field allowed us to distinguish only Γ_3^- from all other possible phonons.

In order to carry the analysis of the symmetry of the coupled phonons a step further, we repeated the same measurements for $SrF_2:Sm^{2+}$. A complete analysis of this system has been reported by Cohen and Guggenheim.[16] Through comparison of our results on $EuF_2:Sm^{2+}$ and $SmCl_2:Sm^{2+}$ with those of $SrF_2:Sm^{2+}$, plus the analysis of the coupling probability (to be discussed in detail in Sec. IV A), and through the direct calculation of the sidebands (to be discussed in Sec. V), we conclude that the symmetry of the coupled phonons is as shown in Table I.

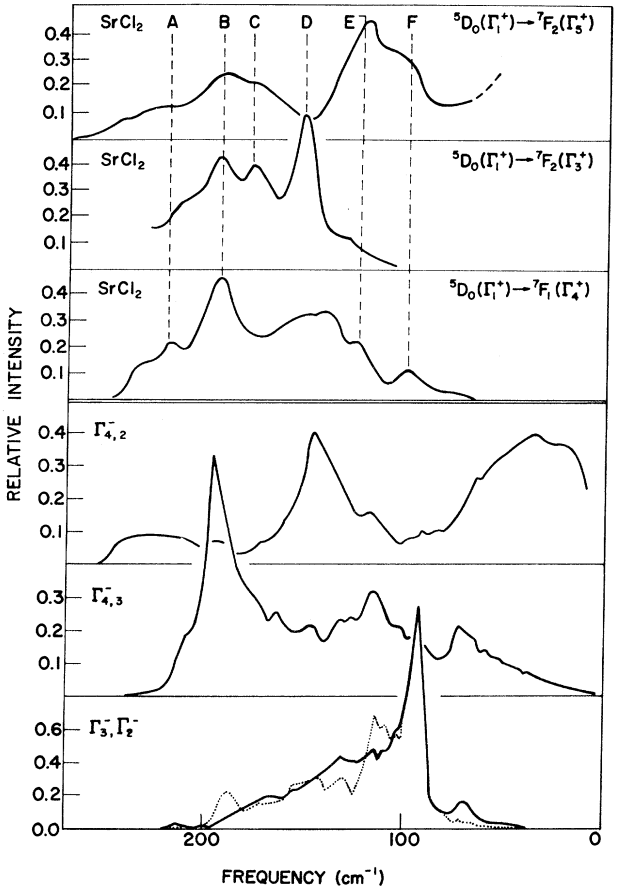

FIG. 4. The upper three curves are the measured sidebands of the $^5D_0(\Gamma_1^+) \rightarrow {}^7F_1(\Gamma_4^+)$, $^7F_2(\Gamma_5^+)$, $^7F_2(\Gamma_3)$ transition of Sm^{2+} in $SrCl_2$. The lower curves are the $\Gamma_{4,2}^-$, $\Gamma_{4,3}^-$, and Γ_3^- and the Γ_2^- (dotted line) sideband calculated with the ASM.

TABLE I. Symmetry type of coupled phonons.

Transition	Observed in $EuF_2:Sm^{2+}$	Observed in $SmCl_2:Sm^{2+}$	Theoretically allowed
$^5D_0 \rightarrow {}^7F_0$	Γ_4^-	Γ_4^-	Γ_4^-
$^5D_0 \rightarrow {}^7F_1$	Γ_4^-	Γ_4^-, Γ_3^-	$\Gamma_5^-, \Gamma_4^-, \Gamma_3^-, \Gamma_1^-$
$^5D_0 \rightarrow {}^7F_2(\Gamma_5^+)$	Γ_4^-, Γ_3^-	Γ_4^-, Γ_2^-	$\Gamma_5^-, \Gamma_4^-, \Gamma_3^-, \Gamma_2^-$
$^5D_0 \rightarrow {}^7F_2(\Gamma_3^+)$	Γ_4^-	Γ_4^-	Γ_5^-, Γ_4^-

IV. THEORY

A. Vibronic Spectra

General theories of vibronic spectra have been formulated by a number of authors.[5,11,18] We follow here the formalism developed by Wagner.[5] Since the pertinent derivations appear in Ref. 5, we state here only that part which is necessary to define relevant parameters and the scope of our calculations.

For 0 °K temperature the one-phonon vibronic sideband, accompanying an electronic transition from an initial state a to a final state b of an optically active ion, is given by the imaginary part of the polarization tensor α:

$$\mathrm{Im}\alpha_{xy}(\omega) = \frac{e^2\hbar}{4\omega} \sum_{\Gamma} \sum_{nn'} \sum_{j} F^{x\Gamma}_{ab,nj}\, \rho^{\Gamma}_{nn'}(\omega) F^{y\Gamma}_{ab,nj} \,, \quad (1)$$

where $\rho^{\Gamma}_{nn'}$ is the projected density

$$\rho^{\Gamma}_{nn'} = \sum_{\vec{k}\lambda} \langle \sigma(n\Gamma j) | \eta(\vec{k}\lambda) \rangle \langle \eta(\vec{k}\lambda) | \sigma(n'\Gamma j) \rangle \, \delta(\omega - \omega(\vec{k}\lambda)) \,. \quad (2)$$

$\omega(\vec{k}\lambda)$ and $\eta(\vec{k}\lambda)$ are the vibrational eigenvalues and eigenvectors of the Sm^{2+}-doped crystal, respectively. $\vec{k}$ is the wave vector of the ideal lattice; λ describes the frequency branches. $\sigma(n\Gamma j)$ is the jth component of the symmetry vector n of the irreducible representation Γ. $F^{i\Gamma}_{ab,nl}$ is given by

$$F^{i\Gamma}_{ab,nj} = \sum_{l} \frac{\langle \Psi_a(\vec{r}) | r_i | \Psi_l(\vec{r}) \rangle \langle \Psi_l(\vec{r}) | V^{\Gamma}_{nj}(\vec{r}) | \Psi_b(\vec{r}) \rangle}{E_l - E_b - \hbar\omega} + \frac{\langle \Psi_a(\vec{r}) | V^{\Gamma}_{nj}(\vec{r}) | \Psi_l(\vec{r}) \rangle \langle \Psi_l(\vec{r}) | r_i | \Psi_l(\vec{r}) \rangle}{E_l - E_a + \hbar\omega} \,. \quad (3)$$

$\vec{r}$ is the electronic position operator measured from the lattice site of Sm^{2+}. (The lattice is assumed to move relative to the Sm^{2+} site.) E_a, E_b, and E_l are the energies of the initial state a, final state b, and intermediate state l.

$V^{\Gamma}(\vec{r})$ is the symmetrized coupling-field operator which for a pure electrostatic electron-phonon interaction is given by

$$V^{\Gamma}_{n\vec{k}}(\vec{r}) = \sum_{m\epsilon s} e^2 \left(Z_{m\epsilon} \frac{r_s - R^0_{m\epsilon s}}{|\vec{r}_s - \vec{R}^0_{m\epsilon s}|^3} - \delta_{00,m\epsilon} \sum_{m'\epsilon'} Z_{m'\epsilon'} \frac{r_s - R^0_{m'\epsilon'}}{|\vec{r}_s - \vec{R}^0_{m'\epsilon' s}|^3} \right) \times \sigma_{m\epsilon s}(n\Gamma\vec{k}) M_{m\epsilon}^{-1/2} \,, \quad (4)$$

where $R^0_{m\epsilon s}$ is the sth component of the equilibrium position vector of the ion ϵ in the unit cell m, $Z_{m\epsilon}$ is the ionic charge, and $M_{m\epsilon}$ is the ionic mass. The second term in the parentheses in Eq. (4) describes the field resulting from the motion of the optically active ion relative to the origin.

As noted earlier, the experimental observations involve four intraconfigurational electronic transitions. From Eq. (3) it is noted that, since the initial a and final b electronic states are of the same parity, the intermediate state and the coupling field must be of odd parity ($\vec{r}$ is an odd-parity operator). When the coupling is purely Coulombic, as will be assumed here for the time being, it becomes useful to expand V in a series of odd-parity multipole fields. Table II indicates the pertinent multipoles and the representation under which they transform in O_h symmetry.

It is assumed that the intermediate states l belong to the nearest odd-parity configuration, i.e., the $4f^5 5d$ configuration. These states are roughly 10 000 cm^{-1} above the $^7F_0(\Gamma_1^+)$ ground state and on the average about 2000 cm^{-1} above the emitting $^5D_0(\Gamma_1^+)$ state.[19] Therefore, the term in Eq. (3) with $|E_l - E_b - \hbar\omega|$ is small compared to the term with $|E_l - E_a + \hbar\omega|$. Experimentally only negligible

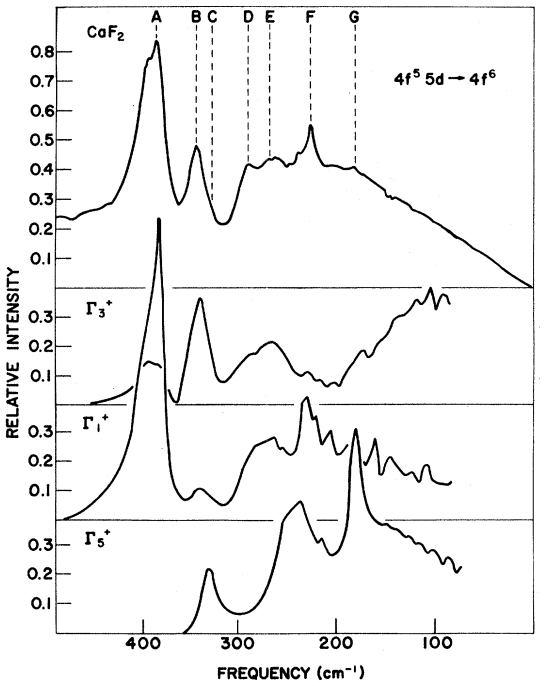

FIG. 5. The upper curve shows the vibronic sidebands of a $4f^5 5d \rightarrow 4f^6$ transition of the Sm^{2+} in CaF_2. The lower three curves are the Γ_3^+, Γ_1^+, and Γ_5^+ calculated sidebands.

intensity is observed in the sideband beyond a phonon frequency of 300 cm^{-1}. It is, accordingly, further assumed that $\hbar\omega$ is small compared to $|E_I - E_a|$. Since the second term in Eq. (3) dominates, and since the initial state a belongs to the Γ_1^+ representation, it follows immediately that the symmetry of the coupling field V, and hence that of the coupled phonon, must be the same as that of the intermediate state.

In order to determine which multipole of V is dominant in the various sidebands, V is next represented in the spherical harmonics Y_N^M up to $N = 5$. In Table II pertinent N values are indicated. Values of N of 1, 3, 5, etc., correspond, respectively, to a dipolar (2^1), octopolar (2^3), and 32-polar (2^5) electrostatic coupling field. It is perhaps valuable to point out immediately that it is unlikely that classical, electrostatic, point-multipole coupling indeed dominates the higher-order (higher than dipolar) coupling. Since the higher-order-coupling volume does not extend beyond the nearest neighbors of the optically active ion, it is more reasonable to assume that classical and quantum-mechanical overlap, spin-orbit, and exchange fields will dominate. We shall return to the basis of this assumption in Sec. V A. It should be noted that this assumption is in contrast to the one made by Wagner[5] which limits intraconfiguration transitions of the Sm^{2+} ion to interactions with electrostatic fields. Whatever the coupling field, it can be expanded in spherical harmonics. It is, accordingly, useful to retain the multipole labels in order to refer to the component of the spherical harmonics involved.

Before proceeding, it is necessary to consider possible admixtures to the electronic wave functions. The final electronic states $^7F_J(\Gamma_i)$ transform in free space according to the total angular momentum J. Since these states belong to the shielded inner $4f$ electronic shell and have energies well below the $4f^5\,5d$ states, it will be assumed that they are not affected by the crystal field. These conditions are, however, not fulfilled for the initial $^5D_0(\Gamma_1^+)$, state and the intermediate states for which admixtures are expected through the presence of the $N = 4$ and $N = 6$ components of the cubic-crystal field.

TABLE II. Decomposition of coupling field.

Phonon symmetry	Coupling field N index of spherical harmonics
Γ_1^-	none < 7
Γ_2^-	3
Γ_3^-	5
Γ_4^-	1, 3, 5
Γ_5^-	3, 5

Table II indicates that under the above assumptions dipole, octopole, and 32-pole coupling is possible. It is possible to estimate the relative strengths of the higher-order Coulombic-coupling fields, by comparing matrix elements of the form $\langle 4f^5\,5d\,|r^N|\,4f^6\rangle$. Judd[20] has tabulated the values of this integral using wave functions of Nd^{3+}. Inserting these values in Eq. (1) shows that the lowest-order coupling will dominate the vibronic sideband structure, when such Coulombic coupling is allowed, even if higher-order Coulombic coupling is made possible through strong admixtures to the initial state. We shall further assume that the same conclusion holds for higher-order fields which are not Coulombic in origin.

Since the symmetry of the coupled phonon must be the same as that of the intermediate state, only Γ_4^- phonons (see Table I) can couple to the $^5D_0(\Gamma_1^+) \rightarrow {}^7F_0(\Gamma_1^+)$ transition. In Table II it is indicated that Γ_4^- phonons can be coupled by either dipolar, octopolar, or 32-polar fields. It will be shown in Sec. V A, by direct calculation of the sideband, that the coupling field in this case is dominantly dipolar in character.

Table I indicates that Γ_1^-, Γ_3^-, Γ_4^-, Γ_5^- phonons can in principle couple to the $^5D_0(\Gamma_1^+) \rightarrow {}^7F_1(\Gamma_4^+)$ transition. If the total angular momentum J is a good quantum number for the initial, intermediate, and final electronic states, then the selection rules require that only dipolar fields can be involved. Table II indicates that in this case only Γ_4^- phonons could couple. However, it can be observed from Fig. 2 that the shape of the sideband accompanying this transition differs from that of the $^5D_0 \rightarrow {}^7F_0$ transition in Fig. 1, which latter has been identified with dipolar coupling. Furthermore, in Table I it is shown that experimentally Γ_3^- phonons are observed to be coupled, which latter phonons can only couple via 32-polar fields (see Table II).

For the $^5D_0(\Gamma_1^+) \rightarrow {}^7F_2\ (\Gamma_5^+)$ transition Table I indicates that Γ_2^-, Γ_3^-, Γ_4^-, Γ_5^- phonons can couple. According to the J selection rule, dipolar and quadrupolar coupling is possible. However, experimentally coupling of Γ_3^- phonons is observed in addition to Γ_4^- phonons.

The coupling of phonons by higher-order fields rules out the possibility that the J selection rules apply in the present case and affirms the assumption made earlier of the existence of crystal-field admixture to the electronic states.

B. Lattice Dynamics

Equations (1)–(3) of Sec. IV indicate the relation of the eigenvectors to the vibronic sideband structure. The next task is to define the lattice dynamics of the Sm^{2+}-doped system. The latter is, in principle, related to the ideal lattice dynam-

TABLE III. Macroscopic parameters.

Macroscopic parameters ($T=0$ °K)	CaF_2	EuF_2	$SrCl_2$	Units
R	2.722×10^{-8} [a]	2.922×10^{-8} *[b]	3.492×10^{12} *[c]	cm
C_{11}	17.400×10^{11} [a]	$12.40\times10^{12}\pm2\%$ [b]	$7.55\times10^{12}\pm5\%$ [b]	dyn/cm^2
C_{12}	5.600×10^{11} [a]	$5.08\times10^{12}\pm2\%$ [b]	$1.72\times10^{12}\pm5\%$ [b]	dyn/cm^2
C_{44}	3.593×10^{11} [a]	$3.18\times10^{12}\pm2\%$ [b]	$1.03\times10^{12}\pm5\%$ [b]	dyn/cm^2
ϵ_∞	2.04 [d]	2.42 [e]	2.7 [c]	
ϵ_0	6.654 [d]	7.52* [f]	1.94* [f]	
$\omega(\Gamma, TO)$	268 [d]	2.03* [e]	155* [c]	cm^{-1}
$\omega(\Gamma, R)$	$330.4\pm1\%$ [g]	$293\pm1\%$ [g]	$187.9\pm1\%$ [g]	cm^{-1}
$\omega(\Gamma, LO)$	484 [d]	358* [e]	248* [h]	cm^{-1}
α_1	1.23×10^{-24} [i]	2.53×10^{-24} [j]	1.55×10^{-24} [j]	cm^{-3}
α_2	6.45×10^{-25} [i]	6.4×10^{-24} [i]	2.974×10^{-24} [i]	cm^{-3}

[a] Reference 23.
[b] Reference 24.
[c] Reference 25.
[d] Reference 26.
[e] Reference 27.
[f] ϵ_0 from room-temperature value measured by one of us (H. V. L.).
[g] Reference 28.
[h] From the Lyddane-Sachs-Teller relation.
[i] Reference 29.
[j] α_1 was calculated from ϵ_∞ and α_2 of Ref. 29.

ics of the pure host lattice.[21,22] We shall restrict our attention to two dynamical models. The first is the shell-deformation model (SDM) introduced by Kühner,[10] which allows ionic polarization as well as radial and axial deformation of the electronic shell. The reduced equation of motion has the form

$$\begin{aligned}\omega\cdot\vec{\eta} &= \underline{A}\cdot\vec{\eta}+\underline{B}\cdot\vec{P}+\underline{C}\cdot\vec{Q}\,,\\ 0 &= \underline{\tilde{B}}^*\cdot\vec{\eta}+\underline{D}\cdot\vec{P}+\underline{E}\cdot\vec{Q}\,,\\ 0 &= \underline{\tilde{C}}^*\cdot\vec{\eta}+\underline{\tilde{E}}^*\cdot\vec{P}+\underline{G}\cdot\vec{Q}\,,\end{aligned} \tag{5}$$

where $\vec{\eta}$ is the mass-reduced ionic displacement, $\vec{P}$ the polarization, and $\vec{Q}$ the deformation of the electronic shell. The reduced-force-constant terms are defined in the Appendix. In addition, we have carried out calculations based on the dynamical model introduced by Axe[23(a)] (ASM), which does not include ionic deformation. The reduced equation of motion for the ASM is obtained by neglecting the ionic deformation $\vec{Q}$ in Eq. (5). (The breathing-shell model introduced by Schroeder[23(b)] is obtained if only radial deformation of the electronic shell is allowed.)

Microscopic parameters such as ionic polarizabilities, force constants, etc., of each model are obtained directly from macroscopic parameters such as the optically observable infrared- and Raman-active frequencies, the elastic constants, the dielectric constants, etc. The values used are indicated in Table III. In certain instances (indicated in Table III by asterisks) the low-temperature data are not available. In this event extrapolation from high-temperature data to 4 °K has been carried out through comparison with similar data for SrF_2 and BaF_2. The parameters of the models are tabulated in Table IV, and their physical meaning indicated in the Appendix. It should be realized that

TABLE IV. Shell-model parameters.

	$A_1(e^2/v)$	$B_1(e^2/v)$	$A_2(e^2/v)$	$B_2(e^2/v)$	$KD1(e^2/v)$	$KD2(e^2/v)$	λ_1^D	λ_2^D	ϵ_∞	Error[a] (%)
					$SrCl_2$					
ASM	33.600	−2.5074	4.2452	0.09487	75.104	34.842	0.081552	−0.18186	2.22	1.0
SDM	34.708	−2.6743	3.4598	0.56011	75.083	34.645	0.26361	−0.11908	2.22	4.1
					EuF_2					
ASM	35.045	−4.6424	0.91538	0.63120	26.995	74.212	0.09252	−0.33398	2.05	1.0
SDM	35.291	−4.7125	1.0334	0.5974	26.998	74.217	0.08175	−0.34473	2.05	1.0
					CaF_2					
ASM	32.626	−4.2033	2.3882	0.3397	31.737	59.525	0.1132	−0.3378	$\epsilon_{expt.}$	2.0

[a] The error is calculated from the sum of all relative deviations from the macroscopic data of Table III, except for ϵ_∞.

in each case, i.e., for CaF_2, EuF_2, and $SrCl_2$, low-temperature neutron-scattering data are *not* available. Therefore, the shell models' parameters have not been fitted to the dispersion curves, as is done in the Cowley-Cochran shell models.[30]

We now turn to the problem of the effect on the ideal lattice dynamics of the presence of the Sm^{2+} ion in the lattice. It may be safely assumed that no observable lattice perturbation exists in the case of $EuF_2:Sm^{2+}$, since in this case the electronic configuration differs only by one $4f$ electron, and the differences in atomic mass and ionic radii are slight.

The situation in $SrCl_2:Sm^{2+}$ is not immediately as clear. It can be readily shown, in the event the coupling field is dipolar or that only even phonons are coupled, that in cubic symmetry the field due to the motion of the optically active ion vanishes. Accordingly, the only possible observable disturbance is that due to changes in the forces between that ion and its neighbors. Although there is no *a priori* reason to expect such, we now show from empirical facts that such force changes must be negligibly small for this case.

For $SmCl_2:Sm^{2+}$, Axe and Sorokin[17] report a sharp vibrational peak at 213 cm^{-1} in the vibronic structure of the absorption spectrum. This structure must be due to even-parity vibrations. It is found from our calculations, assuming no force changes, that the projected density of the Γ_1^+ vibrations of the nearest neighbors has only one sharp peak at 210 cm^{-1}. This maximum accounts for the observations of Axe and Sorokin.[17] We assume, accordingly, that for EuF_2 and $SrCl_2$ the changes in the nearest-neighbor forces in the vicinity of the Sm^{2+} are negligibly small. The direct calculations of the vibronic sidebands, to be discussed in Sec. V, have been carried out using the ideal lattice dynamics of the respective alkaline-earth halide crystals.

V. ANALYSIS

A. Vibronic Spectra

We now turn to a comparison of the experimentally observed vibronic sidebands to the sidebands calculated directly from Eq. (1). Eigenfrequencies, eigenvectors, and the dynamical polarization were calculated for 326 $\vec{k}$ vectors in $\frac{1}{48}$ of the first Brillouin zone.[31] The small number of calculated solutions lead to unimportant uncertainties in the low-frequency region. Three types of coupling fields have been employed. These are (i) an electrostatic dipolar field, (ii) an electrostatic octopolar field (used for EuF_2 only), and (iii) a field which can couple independently to various components of the vibrational modes of the Sm^{2+} ion and its nearest neighbor. The latter simulates a highly localized higher-order coupling field. The actual form of the latter field can be viewed as some unspecified combination of the multipole fields. We shall refer to this as the "nearest-neighbor field." It will be shown that the calculated sidebands further strengthen the assignments of the symmetry of the coupled phonons and the apparent order of the coupling field as given in Sec. IV A.

1. EuF_2

In Fig. 1 are shown the experimentally observed [curve (a)] and theoretically calculated [curves (b)–(d)] vibronic structure which accompanies the $^5D_0(\Gamma_1^+) \rightarrow {}^7F_0(\Gamma_1^+)$ of Sm^{2+} in EuF_2. The theoretical calculation for this and other transitions is based on the SDM. The calculations have been repeated for the ASM (not shown in Fig. 1). No appreciable difference is observed. The vibronic sideband is calculated on the assumption of a pure-electrostatic dipolar-coupling field. Curve (b) shows the results based on the macroscopic parameters taken from Table III. It can be seen that the calculated frequencies of the major maxima are about 15–20 wave numbers lower than those observed experimentally. Kühner[10] has reported obtaining the same result in the $SrF_2:Sm^{2+}$ and $BaF_2:Sm^{2+}$ systems. It is shown that this discrepancy can be consistently removed by lowering the cation polarizability by approximately 20%. Within the context of the model this reduction implies a concurrent reduction in the high-frequency dielectric constant (see Ref. 29). A similar reduction in the Eu^{2+} polarizability results in curve (d) in Fig. 1. Curve (c) contains the result of a calculation in which the coupling resulting from dynamical polarization is artificially suppressed. Comparison of curves (c) and (d) yields an indication of the contribution that polarization makes to the sideband structure. It can be seen that its inclusion leads to an over-all improvement in the relative intensities. It should particularly be noted that the sideband is satisfactorily described by electrostatic dipolar coupling.

In Fig. 2 are plotted the experimental and calculated vibronic structure accompanying the $^5D_0(\Gamma_1^+) \rightarrow {}^7F_1(\Gamma_4^+)$, $^7F_2(\Gamma_3^+)$, and $^7F_2(\Gamma_5^+)$ transitions. Theoretical sidebands have been calculated on the basis of electrostatic octopolar coupling (not shown) and on the basis of the nearest-neighbor field.

Vibronic structure calculated solely on the basis of electrostatic dipolar or octopolar fields does not correspond to the observed structure for these transitions. Octopolar coupling leads, in addition, to unobserved intensity in the lower-acoustic-frequency region. Considerably better agreement is, however, obtained if the nearest-neighbor coupling

field is used. The latter results are discussed below.

The theoretical sidebands shown in Fig. 2 are those due to Γ_3^- and to two Γ_4^- vibrations of the nearest neighbors, providing that these vibrations are independently coupled to the electronic transition. It is useful to distinguish the three components of the vibrations which correspond to the Γ_4^- vibrations of the Sm^{2+} ion plus its eight nearest neighbors. Accordingly, we distinguish between a $\Gamma_{4,1}^-$ vibration which is that of the Sm^{2+} ion itself, a $\Gamma_{4,2}^-$ vibration which is a transverse motion of the nearest neighbors, and a $\Gamma_{4,3}^-$ vibration which corresponds to the remaining possible Γ_4^- vibration of the nearest neighbors.

By comparison with Fig. 1 it is seen that maximum B is mainly due to a remnant of the dipolar coupling field. The same is true for maximum D. Based on the similarity of the structure in the acoustic region, we assign the $\Gamma_{4,3}^-$ vibration to that region of the ${}^5D_0(\Gamma_1^+) \rightarrow {}^7F_2(\Gamma_5^+)$ sideband. The latter vibration produces no shift in the center of mass of the nearest-neighbor halides, contrary to the case of the $\Gamma_{4,2}^-$ vibration. A stronger coupling of the $\Gamma_{4,2}^-$ vibration is accordingly expected: a fact which is indeed observed by the appearance of maximum E in all three sidebands. The intensity of the $\Gamma_{4,3}^-$ vibration in the lowest-frequency acoustic region is found theoretically to cancel out with the vibration of the Sm^{2+} itself, stemming from the fact that these two modes possess only a very small relative phase shift in this frequency region. Maximum G of the ${}^5D_0 \rightarrow {}^7F_1(\Gamma_4^+)$ sideband is uniquely produced by the $\Gamma_{4,1}^-$ vibration.

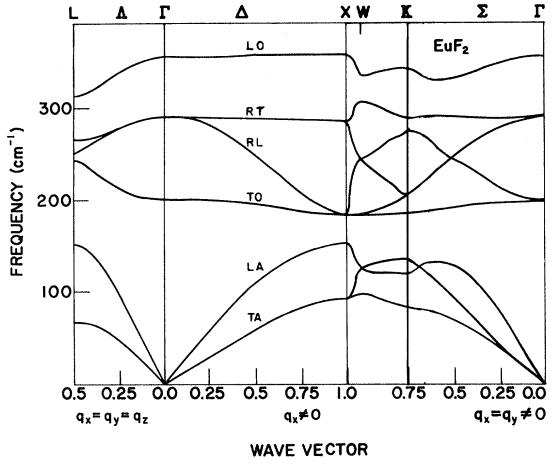

FIG. 6. Dispersion curves for EuF_2 based on the SDM. The representation deviates from the standard one. Included is the path along the zone face from the X point over the W point to the K point. RT and RL refer to the Raman transverse and Raman longitudinal branches, respectively.

In addition to the coupling described above, even higher-order coupling is apparently also observed. The maximum F in the ${}^5D_0 \rightarrow {}^7F_2(\Gamma_5^+)$ sideband corresponds to the sharp maximum in the Γ_3^- density. The latter vibration couples, according to Table II, over a 2^5-polar field. The symmetry assignment is in agreement with the experimentally observed polarization in this region of the sideband.

Of course it is possible that, in addition, a weak coupling of Γ_1^-, Γ_2^-, and Γ_5^- vibrations also exists. Considerable coupling of these modes can, however, be ruled out for the $EuF_2:Sm^{2+}$ system by the following arguments. The Γ_2^- and Γ_5^- modes can be excluded because they would produce unobserved maxima in the acoustic or in the region of the longitudinal-optic branch. The Γ_1^- mode is excluded by the fact that there is no Γ_1^- vibration of the nearest neighbors and that the coupling field is 2^7-polar or higher as can be seen from Table II. Since such fields must be highly localized about the Sm^{2+} ion, it is very unlikely that this coupling is observable.

Two-phonon coupling is also observed in the region of the one-phonon sideband. In Fig. 6 is shown the frequency dependence of the density of states of EuF_2 as calculated from the SDM. A frequency gap can be observed between the acoustic and the optic modes. Also observable is a region of very low density between the region of the longitudinal-optic branch and the other optic branches. These gaps are, in fact, observed experimentally in the sideband of the ${}^5D_0 \rightarrow {}^7F_0$ transition. In contrast, the other sidebands show considerable intensity in these frequency regions (see maximum A_1 in Fig. 2). It is possible that the maximum C also results from two-phonon coupling. It cannot be accounted for solely by one-phonon coupling.

2. $SrCl_2$

The theoretical curves of Figs. 3 and 4 are based on the ASM. Similar curves have been calculated based on the SDM. As is the case with EuF_2, no appreciable difference is observed. The analysis of the vibronic structure accompanying the transition of Sm^{2+} in $SrCl_2$ closely follows that given above for EuF_2 with the following exceptions.

The inclusion of dynamical polarization in the calculation of the sideband of the ${}^5D_0 \rightarrow {}^7F_0$ transition leads to an experimentally unobserved maximum in the transverse-acoustic region. A possible source of this disagreement will be discussed in Sec. VI.

As can be seen from Fig. 4, the ${}^5D_0(\Gamma_1^+) \rightarrow {}^7F_2(\Gamma_5^+)$ sideband is mainly a combination of the $\Gamma_{4,3}^-$ and the Γ_2^- vibrations. The latter vibration, which was not detected in $EuF_2:Sm^{2+}$ system, appears to be required here in order to account for the additional maximum near the maximum E. The Γ_3^- vibration, which also could account for the additional maxi-

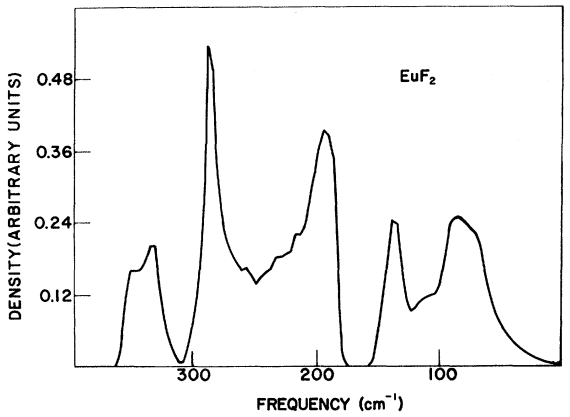

FIG. 7. Frequency density of EuF_2 based on the SDM.

mum, was not detected by polarization measurements (contrary to the $EuF_2:Sm^{2+}$ case). The main peak of the ${}^5D_0(\Gamma_1^+) \rightarrow {}^7F_2(\Gamma_3^+)$ transitions is mainly due to the $\Gamma_{4,2}^-$ vibration. Maxima A and B are due to dipolar coupling. Maximum C is too strong to be explained only by dipolar coupling. The components of the sideband of the ${}^5D_0(\Gamma_1^+) \rightarrow {}^7F_1(\Gamma_4^+)$ transition are the same as those of the ${}^5D_0(\Gamma_1^+) \rightarrow {}^7F_2(\Gamma_3^+)$ transition, except that maxima F and E are due to the Γ_3^+ vibration, as is indeed predicted by the polarization measurements.

One further, but important, difference exists between the analysis of $SrCl_2:Sm^{2+}$ and the $EuF_2:Sm^{2+}$ systems. This has to do with the assignment of the energy of the ${}^5D_0(\Gamma_1^+) \rightarrow {}^7F_2$ (Γ_3^+) and the ${}^5D_0(\Gamma_1^+) \rightarrow {}^7F_2(\Gamma_5^+)$ electronic transitions. The assignment is complicated to some extent by some overlapping of the accompanying vibronic sidebands. We obtain the best agreement (discussed in the preceding paragraph) if we assume that the ${}^7F_2(\Gamma_3^+)$ state lies lower in energy than the ${}^7F_2(\Gamma_5^+)$ state. This is contrary to the situation normally observed in the alkaline-earth fluorides, but is in agreement with what is expected from simple, zero-order, crystal-field theory.

3. CaF_2

As noted earlier, the one-phonon sideband accompanying the dipole-allowed $4f^5\,5d \rightarrow 4f^6$ transition of Sm^{2+} in CaF_2 is limited to even-parity phonons. Two-phonon structure, which is also observed, is not so limited. We shall not be concerned with the latter here. Even phonons are coupled over monopole or higher-order even-polarity fields. Since such fields are local in character, we assume for simplicity that only even vibrations of the nearest neighbors are important. We further limit attention to those vibrations which involve essentially radial motion of the nearest-neighbor ions, since these are expected to be more strongly coupled than tangential vibrations. These are the Γ_1^+, Γ_3^+, and one of the Γ_5^+ vibrations.

In Fig. 5 we compare the measured sideband in the one-phonon region with the theoretical sidebands. Maximum A and maximum B are very well reproduced by the Γ_1^+ and Γ_3^+ sidebands. Maxima D and E correspond to Γ_3^+ vibrations, whereas the characteristic maximum F is due to Γ_1^+ vibrations. The small peaks C and G may be due to the Γ_5^+ vibrations, although these vibrations are of minor importance. Electrostatic quadrupole coupling allows only coupling of Γ_3^+ and Γ_5^+ vibrations. The observed strong Γ_1^+ coupling is, therefore, due to monopole or a higher-order coupling.

Maximum B, as well as A, are calculated to lie slightly at lower frequencies than observed experimentally. This discrepancy could have been removed by decreasing the polarizability of the cation in a fashion equivalent to the procedure used for EuF_2 and $SrCl_2$. However, the difference between the ionic radii[32] of Sm^{2+} (~1.29 Å) and Ca^{2+} (0.99 Å) may involve an appreciable increase of the force constants to the nearest neighbors, which may equally well account for an increase of the frequencies.

B. Ideal Lattice Dynamics

In Figs. 6 and 7 we present dispersion curves and the one-phonon density of EuF_2 as derived solely from the model parameters of the SDM and the vibronic spectra. Similar results are shown in Figs. 8 and 9 for $SrCl_2$ for which the Axe model was used. No neutron-scattering data currently exist to check the predicted dispersion curves. In the absence of such direct data, we now carry out an estimation of the inherent error, in the predicted dispersion relations, in terms of the vibronic data.

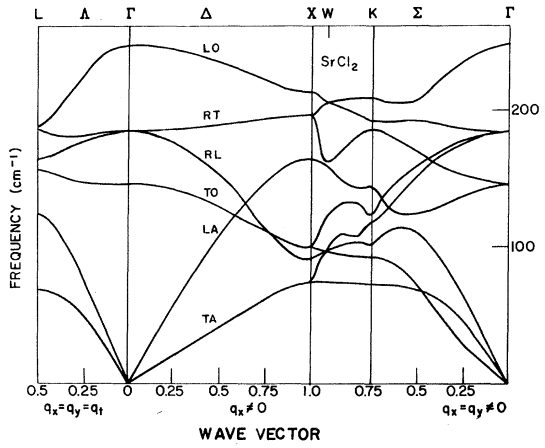

FIG. 8. Dispersion curves for $SrCl_2$ based on the ASM.

Equations (1) and (2) reveal that the structure of the vibronic spectra depends on three quantities: the coupling field F, the eigenvalue $\omega(k\lambda)$, and the eigenvector $\vec{\eta}(k\lambda)$. The eigenvector is directly related to the polarization vector $\vec{\epsilon}(k)$ by

$$\vec{\eta}_m(\vec{k}\,\lambda) = \epsilon(\vec{k}\lambda) e^{i\vec{k}\cdot\vec{R}^0_m}.$$

Accordingly, the error in the present results may originate from the following three sources: (i) error in the dispersion relation, (ii) error in the polarization vector, and (iii) error in the coupling field.

In Sec. V A 1 we have shown that the vibronic sideband of the $^5D_0 \rightarrow {}^7F_0$ transition of Sm^{2+} in EuF_2 can be very well accounted for in terms of a dipolar coupling field. If we assume that this is exactly the case, then the error must reside in the dispersion relation and the polarization vector.

Errors in the polarization vectors lead to incorrect intensities in the vibronic spectra, whereas errors in the dispersion relations can be most readily detected in incorrect frequencies of various features of the spectra. It is known from the perturbation theory of eigenvalue problems that small errors in the dynamical matrix lead to smaller errors in the dispersion relation than in the eigenvectors. It follows that the error in the dispersion relations can be estimated from a comparison of the frequency of the calculated and measured maxima as long as the average error in the intensities is of the same magnitude as that of the frequencies.

In the case of $EuF_2:Sm^{2+}$, Fig. 2 shows that the maximum E is calculated to be approximately 3% lower in frequency than observed. In Fig. 1 it is shown that the gap between acoustic and optic modes is shifted to slightly lower frequencies. The latter discrepancy apparently stems from a too low optic-transverse frequency. The low-temperature value for this frequency was estimated from high-temperature data and from the temperature dependence of this frequency in other alkaline-earth halides. We estimate on the basis of the over-all agreement between observed and calculated vibronic structure in the $EuF_2:Sm^{2+}$ system that the error in individual eigenvalues is on the average 3%. The average error in the intensities is 6%, as determined from the ratio of the area between the calculated and measured structure to the area of the measured structure. We conclude that the average error in the predicted dispersion curves is approximately 3% for this system.

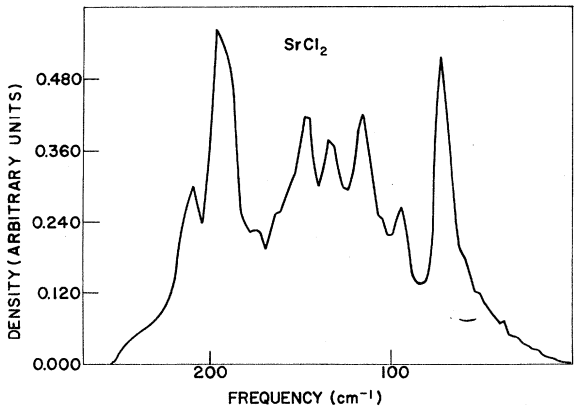

FIG. 9. Frequency density of the $SrCl_2$ based on the ASM.

The experimental values for the elastic constants of $SrCl_2$ are attached with an error of 4%.[24] The low-temperature infrared-active optical frequency is again estimated from high-temperature data. The over-all mismatch of the frequency of the various peaks in Figs. 3 and 4 is not more than 5%. As will be discussed in Sec. VI, the coupling field in this system is not as well understood as in the $EuF_2:Sm^{2+}$ system. Based solely on the frequency mismatch, we estimate an average error of 5% in the dispersion curves. The real error may be somewhat higher.

From the discussion in Sec. V A 3, it follows that local perturbations may be responsible for the mismatch observed for the calculated and measured sidebands of Sm^{2+} in CaF_2. Therefore, a judgment of the quality of the predicted dispersion curves of CaF_2 at $T=0$ is not possible. Comparison between the calculated low-temperature dispersion curves and those measured at high temperature shows that the main difference is a shift to higher frequencies at low temperature.

A comparison also can be made of the error inherent in calculations based on the SDM and ASM and those generally obtained from calculations using Cowley-Cochran[30] shell models. It should be kept in mind that the error quoted for the present calculations is based on a determination involving a sum of contributions from phonons with k vectors from all parts of the Brillouin zone. A comparison with results based on phonons of a known, but restricted, set of k vectors along symmetry directions, such as the dispersion curves normally published from neutron-scattering experiments, is therefore not particularly meaningful. A more useful comparison can, however, be made with results from perturbation-induced infrared absorption[33] and Raman-scattering[34] experiments. Timusk and Ward[33] have found that the frequency of structure in the defect-induced infrared absorption of KBr can be reproduced to within 5% by the Cowley-Cochran model. In a recent paper by Harley, Page, and Walker,[34] on calculations based on the Cowley-Cochran model and results obtained from perturbation-induced Raman scattering in the alkali halides, deviations of 4–5% are observed which cannot be

explained by defect-induced distortions. We conclude that the error inherent in the Cowley-Cochran method is of the same magnitude as that inherent in the method used here.

VI. DISCUSSION

We have used vibronic sidebands of Sm^{2+} in EuF_2, $SrCl_2$, and CaF_2 to test the shell-deformation model introduced by Kühner[10] and the model introduced by Axe.[23] We have shown by fitting independently obtained macroscopic data that excellent agreement between calculated and measured sidebands can be reached. The calculations represent, with two exceptions, an *ab initio* determination of the ideal lattice dynamics of the host lattices. One exception is that the inclusion of dynamical polarization does not always lead to an improvement of the intensities of calculated as compared to the experimental sidebands. In the case of $SrCl_2:Sm^{2+}$ it leads, in addition, to experimentally unobserved structure in the 70-cm^{-1} region. A second exception is that the calculations lead to values of the high-frequency dielectric constant which are approximately 15% lower than experimental values. Similar deviations are obtained with the Cowley-Cochran models[30] for the alkali halides. In the latter systems the calculated dielectric constants tend to be 5% smaller than the experimental values.[35(a)] Recently, a discrepancy as high as 35% has been reported for RbBr.[35(b)]

The discrepancies cannot be removed with the more sophisticated shell-deformation model instead of the simpler Axe model. Both models lead to very similar results, and the necessity to include deformation effects in a model for the ideal lattice dynamics of alkaline-earth halides could not be proved. We have, therefore, to consider the observed overestimation of the polarization as a breakdown of some basic assumption of the shell models. In a preceding paper, Kühner[8] has enumerated the approximations necessary to obtain a system of equations of motion which is in one-to-one correspondence with the shell-model equations (see also the Appendix). One of the assumptions is that the charge distributions of the ions are well separated and that a point-multipole expansion is valid.

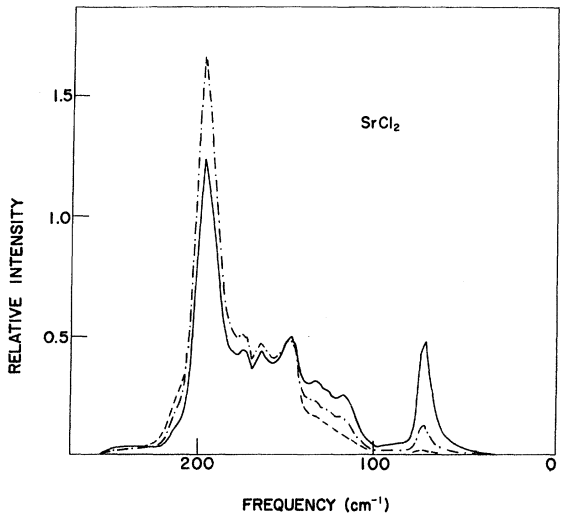

FIG. 10. Calculation of $^5D_0 \rightarrow {}^7F_0$ of Sm^{2+} in $SrCl_2$ including the effects of charge overlap. Curve (a) (dashed line) is the calculated sideband for $R = 0.1a$. Curve (b) (solid line) is the $R = 0.7a$ case; curve (c) (dashed line) is the $R = 0.9a$ case. R is given in units of the nearest-neighbor distance.

We consider in truly ionic crystals that the electronic charge distributions of unpolarized ions are well separated. Even for such crystals, however, we expect that polarization involves some extension of the spacial distribution of charge due to admixtures of excited, or charge transfer, states. The effects of extended charge need, accordingly, to be considered even for the nominally ionic crystals investigated here. In order to demonstrate this point, we have performed a crude model calculation of the vibronic sideband accompanying the $^5D_0 \rightarrow {}^7F_0$ transition of Sm^{2+} in $SrCl_2$. In the calculation of the electron-phonon coupling (but not in the lattice dynamics), we have substituted for the point-dipole charge an extended-dipolar charge distribution $\rho(r)$. The polarization then is

$$\vec{P}_{m\epsilon}(r, \vec{k}\lambda) = \vec{P}_{m\epsilon}(\vec{k}\lambda)\rho(r) , \tag{6}$$

where $\vec{P}_{m\epsilon}(\vec{k}\lambda)$ is the polarization normally used in the shell models. $\rho(r)$ is chosen to be constant within a sphere of radius R and zero for $r > R$. For additional simplicity we set $\rho(r)$ equal for cation and anion.

In the event that both distributions do not overlap, then the only difference with the point-dipole approximation is a finite electrostatic interaction between the dynamical polarization of the optically active ion and its electrons. To demonstrate this case we have assumed that $R = 0.1a$, where a is the nearest-neighbor distance. The result is plotted in curve (a) of Fig. 10. It can be seen from comparison with curve (b) of Fig. 3 that this does not lead to any noticeable changes. This situation may change for higher than the dipolar coupling. The effect of considerable overlap is simulated by setting $R = 0.7a$ [see curve (b) in Fig. 10]. Comparison of this result with experiment [curve (a) in Fig. 3] shows that overlapping effects tend to decrease the intensitites in the 0–120-cm^{-1} region. In particular, the intensity of the unobserved maximum is considerably reduced. For $R = 0.9a$ the unobserved maximum disappears and the resulting curve (c) is similar to the rigid-ion case

[Fig. 3, curve (c)]. It is seen that charge overlap reduces the interaction between polarized ions. The effect is to reduce the effective field at a polarized ion resulting from the polarization of its neighbors. Nevertheless, the total macroscopic polarization remains unchanged, as would the experimentally determined dielectric constant. It would be expected, and is indeed observed,[35] that the effect is more noticeable in alkaline-earth halides as compared to alkali halides, since in the former short-range overlap forces are about three times stronger. Thus, the previously noted discrepancy in the dielectric constant may be accounted for.

It should be noted that information on the overestimation of the polarization by the shell models is inherent in the vibronic spectra from the fact that the intensities of various features of the spectra are related to the dynamical eigenvectors. Vibronic spectra, therefore, constitute a critical test of the dynamical models.

It is also worth noting that Sinha[36] has shown, for semiconductor crystals with considerable charge overlap, that the dynamics of such systems can be recast into a set of equations which formally have the same structure as the shell-model equations, and which reduce completely to the equations used here if point-dipole charges are imposed. This indicates that even in the presence of strong overlap, the formal structure of the shell models can be maintained, although (of course) the interpretation of the various model parameters changes.

With regard to the nature of the electron-phonon-coupling field, it is observed that only the $^5D_0 \rightarrow {}^7F_0$ transition of Sm^{2+} is coupled to a dipolar field which is most likely electrostatic in origin. The other $4f \rightarrow 4f$ transitions observed involve coupling to higher-order fields which do not originate from electrostatic point-multipole fields. It is further observed that the latter fields must be highly localized about the Sm^{2+} ion. We suspect that these fields originate from overlap, spin-orbit, or exchange interactions.

VII. CONCLUSION

We have demonstrated that a study of vibronic spectra yields information on ideal lattice dynamics. The analysis yields the dispersion relationships of the lattices and constitutes a stringent test of the dynamical eigenvectors, and of the dynamical model employed. In addition, we are able to identify the symmetry and physical nature of the electron-phonon-coupling field. In contradiction to previous assumptions that the $4f \rightarrow 4f$ electronic transitions of the Sm^{2+} probe ion are coupled only to point-multipole electrostatic fields, we suspect that the electron-phonon interaction includes short-range overlap, exchange, or spin-orbit effects.

APPENDIX

In the quantum-mechanical theory of lattice dynamics, developed in Ref. 8, it is shown that the following assumptions and restrictions have to be made in order to establish simple shell models.

(i) The dynamical change of the charge distribution of any two neighboring vibrating ions is such that the total charge pertaining to each individual ion is not altered [see Ref. 8, Eq. (64)]. This means that there is no dynamical charge transfer between the ions.

(ii) The $\vec{k}$ dependence of the energy gap between the conduction and valence band is small compared to the mean value of the gap [see Ref. 8, Eq. (62)].

(iii) Overlapping of the electronic wave functions is small and a two-center approximation can be introduced.

(iv) The dynamical change of the local charge distribution of an ion is developed in a hierarchy of moments. The lowest-order approximation would be to keep only the dipole moment:

$$\vec{P}_{m\epsilon} = \int \Delta\rho_{m\epsilon}(\vec{r})\vec{r}\, d\tau \quad , \tag{A1}$$

where ϵ is the index of the ion in the unit cell m, and r is the electronic coordinate. This would lead to the Cochran model (CSM). The next approximation is to include the moments of the deformation:

$$Q_{m\epsilon x} = \int \Delta\rho_{m\epsilon}(\vec{r}) r_x^2\, d\tau, \quad Q_{m\epsilon y},\ Q_{m\epsilon z},\ \text{cyclical.} \tag{A2}$$

This leads to the shell-deformation model (SDM).

(v) The pseudopotentials describing the overlap and exchange interaction between the ions are in principle different for each electronic transition. Within the set of all odd transitions and within the set of all even transitions, we neglect these differences (see the Appendix of Ref. 8).

(vi) The average pseudopotentials themselves are functions of the dynamical change of the charge distribution. We include this effect in a moment expansion which includes the moments of Eqs. (1) and (2).

All these approximations permit a description of the behavior of the ions, under the influence of the short-range forces, by a tensor of the polarizability [see Ref. 8, Eq. (77)] and by a tensor $\gamma_\epsilon^{xx,yy}$ which describes the deformability per ion ϵ. This tensor has, in cubic symmetry, only two different elements, which describe the radial and axial deformation of the ion ϵ. All shear deformation ($\gamma_\epsilon^{xy,xy}$) is neglected.

For further simplification we assume that all pseudopotentials are central-force potentials. The force-constant matrix N^D describing the interaction between two polarized ions is then

$$N^D(00i, m\epsilon j) = -A' \frac{R^0_{m\epsilon i} R^0_{m\epsilon j}}{|R^0_{m\epsilon}|^2} - B' \left(\delta_{ij} - \frac{\vec{R}^0_{m\epsilon i} \vec{R}^0_{m\epsilon j}}{|R^0_{m\epsilon}|^2}\right). \tag{A3}$$

In order to describe the interaction produced by the dipole moment P of a polarized ion and deformation moment Q of a deformed ion, we need an additional three parameters.[37] For the deformation-deformation moment interaction we need another four parameters.[37] At this point it should be noted that 24 parameters would be required to describe the short-range interaction between two different ions and 16 parameters between two identical ions. In order to reduce the number of parameters, we note that the short-range interaction decreases in R with a power between 6 and 12.[38] Therefore, only the two highest derivatives of the pseudopotential are important. Accordingly the force-constant matrix of the short-range interaction between a polarized ion at the origin and deformed ion $m\epsilon$ is

$$N^Q(00k, m\epsilon i) = -(A'' - 3B'') \frac{R^0_{m\epsilon k} R^{0\,2}_{m\epsilon i}}{|R^0_{m\epsilon}|^2} - B'' \frac{1}{|R^0_{m\epsilon}|} (\vec{R}^0_{m\epsilon k} + 2\vec{R}^0_{m\epsilon i}\delta_{ik}) \tag{A4}$$

and the matrix of the short-range interaction between two deformed ions is

$$N^Q(00i, m\epsilon j) = -(A'' - 6B''') \frac{R^0_{m\epsilon i} R^{0\,2}_{m\epsilon j}}{|R^0_{m\epsilon}|^4} - B''' \frac{1}{|R^0_{m\epsilon}|^2} \times (R^{0\,2}_{m\epsilon i} + R^{0\,2}_{m\epsilon j} + 4R^0_{m\epsilon i} R^0_{m\epsilon j}\delta_{ij}) . \tag{A5}$$

We further assume that the Coulombic interaction is included in A'', B'' and A''', B'''. Accordingly, the required parameters have been reduced by three.

The short-range-force-constant matrix, due to the motion of the rigid ions from their equilibrium position, is given by a matrix of the form of Eq. (3). However, in this case we assume a noncentral-force potential. The short-range interaction between a polarized, or deformed, ion $m\epsilon$ and the moving ion at the origin is represented in the form of Eqs. (4) and (5), respectively.

In order to further reduce the number of different parameters, we assume that the force constants of the short-range interaction $F(\kappa', \kappa)$, which are due to the displacement of the two rigid ions κ and κ', differ only by a factor of proportionality $\lambda^D_{\kappa'}$ from the force constants $N(\kappa, \kappa')$ of the short-range interaction, which is produced by the displacement of the ion, κ, in the ground state from the equilibrium position and by the polarization of the ion κ'. Entirely in the same way, the force constants of $N^D(\kappa, \kappa')$ which are produced by the polarization of the ion κ and κ' differ from $N(\kappa, \kappa')$ only by a factor λ^D_κ. This approximation is equivalent to the assumption of Cochran *et al.*[35] that the short-range interaction between the shells and the ions and between the shells are equal. In accordance with this concept, we introduce λ^0_κ as the force constant of shell deformation. Accordingly, the number of required parameters is reduced to six for the fluorite structure.

The reduced equation of motion of the general SDM has then the following form:

$$\begin{aligned}
M_\epsilon \omega^2(\vec{k}\lambda)\, \Delta R_{\epsilon x}(\vec{k}\lambda) &= \sum_{\epsilon j} \{[F(\vec{k}, \epsilon x, \epsilon_1 j) + Z_\epsilon C(\vec{k}, \epsilon x, \epsilon_1 j) Z_{\epsilon_1}]\Delta R_{\epsilon_1 j}(\vec{k}\lambda) \\
&\quad + [F(\vec{k}, \epsilon x, \epsilon_1 j)\lambda^D_{\epsilon_1} + Z_\epsilon C(\vec{k}, \epsilon x, \epsilon_1 j)] P_{\epsilon_1 j}(\vec{k}\lambda) \\
&\quad + FQ(\vec{k}, \epsilon x, \epsilon_1 j)\lambda^Q_{\epsilon_1} Q_{\epsilon_1 j}(\vec{k}\lambda)\}, \\
0 = \sum_{R_{ij}} \lambda^D_\epsilon [\tilde{F}^*(\vec{k}, \epsilon x, \epsilon_1 j) + \tilde{C}^*(\vec{k}, \epsilon x, \epsilon_1 j) Z_{\epsilon_1}]\, \Delta R_{\epsilon_1 j}(\vec{k}\lambda) \\
+ [\lambda^D_\epsilon F(\vec{k}, \epsilon x, \epsilon_1 j)\lambda^D_{\epsilon_1} + KD_{\epsilon_1}\delta_{\epsilon_1}\delta_{xj} + C(\vec{k}, \epsilon x, \epsilon_1 j)] R_{\epsilon_1 j} \\
+ \lambda^D_\epsilon \tilde{F} Q(\vec{k}, \epsilon x, \epsilon_1 j)\lambda^Q_{\epsilon_1} Q_{\epsilon_1}(\vec{k}\lambda), \qquad \text{(A6)} \\
0 = \sum_{\epsilon_1 j} \lambda^Q_\epsilon \tilde{F} Q^*(\vec{k}, \epsilon x, \epsilon_1 j)\, \Delta R_{\epsilon_1 j}(\vec{k}\lambda) \\
+ \lambda^Q_\epsilon \tilde{F} Q^*(\vec{k}, \epsilon x, \epsilon_1 j)\lambda^D_{\epsilon_1} P_{\epsilon_1 j}(\vec{k}\lambda) \\
+ [\lambda^Q_\epsilon QFQ(\vec{k}, \epsilon x, \epsilon_1 j)\lambda^Q_{\epsilon_1} KQ^{xj}_{\epsilon_1}\delta_{\epsilon_1\epsilon}] Q_{\epsilon_1 j}(\vec{k}\lambda),
\end{aligned}$$

where $\Delta R_{\epsilon x}(\vec{k}\lambda)$, $P_{\epsilon_1 j}(\vec{k}\lambda)$, and $Q_{\epsilon j}(\vec{k}\lambda)$ are the polarization vectors of $\vec{R}$, $\vec{P}$, and $\vec{Q}$. Z is ionic charge and C is the reduced-force-constant matrix given by Srinivasan.[39]

With the abbreviations

$$C_x = \cos(qx\pi), \quad S_x = \sin(qx\pi), \quad \text{cyclical} \tag{A7}$$

$$C_{x_2} = \cos(\tfrac{1}{2}qx\pi), \quad S_{x_2} = \sin(\tfrac{1}{2}qx\pi), \quad \text{cyclical} \tag{A8}$$

we obtain for the reduced-force-constant matrices

$$\begin{aligned}
&F(\vec{k}, 1x, 1x) = \tfrac{4}{3}(A_1 + 2B_1), \\
&F(\vec{k}, 1x, 2x) = -\tfrac{2}{3}(A_1 + 2B_1)(C_{x_2}C_{y_2}C_{z_2} - iS_{x_2}S_{y_2}S_{z_2}), \\
&F(\vec{k}, 1x, 3x) = F^*(\vec{k}, 1x, 2x), \qquad \text{(A9)} \\
&F(\vec{k}, 2x, 2x) = F(\vec{k}, 3x, 3x) = [\tfrac{2}{3}(A_1 + 2B_1) + (A_2 + 2B_2)], \\
&F(\vec{k}, 2x, 3y) = 0, \\
&F(\vec{k}, 1x, 2y) = \tfrac{2}{3}(A_1 - B_1)^*(-S_{x_2}S_{y_2}C_{z_2} + iC_{x_2}C_{y_2}S_{z_2}), \\
&F(\vec{k}, 1x, 3y) = F^*(\vec{k}, 1x, 2y); \\
&FQ_N(\vec{k}, \kappa x, \kappa x) = FQ_N(\vec{k}, \kappa x, \kappa y) = 0, \\
&FQ_N(\vec{k}, 1x, 2x) = -\tfrac{2}{3}(1/\sqrt{3})(A_1 + 6B_1) \\
&\qquad \times (-C_{x2}S_{y_2}S_{z_2} + iS_{x_2}C_{y_2}C_{z_2}), \\
&FQ_N(\vec{k}, 2x, 3x) = -iA_2 S_x, \\
&FQ_N(\vec{k}, 1x, 2y) = -A_1(2/3\sqrt{3}) \\
&\qquad \times (-C_{x2}S_{y_2}S_{z_2} + iS_{x_2}C_{y_2}C_{z_2}), \\
&FQ_N(\vec{k}, 1x, 3y) = FQ_N(\vec{k}, 1x, 2y), \qquad \text{(A10)}
\end{aligned}$$

$$FQ_N(\vec{k}, 1y, 2x) = -A_1\,(2/3\sqrt{3}) \times (-S_{x_2}C_{y_2}S_{z_2} + iC_{x_2}S_{y_2}C_{z_2})\,,$$
$$FQ_N(\vec{k}, 1y, 3x) = FQ_N^*(\vec{k}, 1y, 2x)\,,$$
$$FQ_N(\vec{k}, 2x, 3y) = -iB_2S_x\,;$$
$$QFQ(\vec{k}, 1x, 2x) = -\tfrac{2}{9}(A_1 + 12B_1) \times (C_{x_2}C_{y_2}C_{z_2} - iS_{x_2}S_{y_2}S_{z_2})\,,$$
$$QFQ(\vec{k}, 2x, 3x) = -A_2C_x\,, \qquad \text{(A11)}$$
$$QFQ(\vec{k}, 1x, 2y) = -\tfrac{2}{9}A_1\,(C_{x_2}C_{y_2}C_{z_2} - iS_{x_2}S_{y_2}S_{z_2})\,,$$
$$QFQ(\vec{k}, 2x, 3y) = -B_2(C_x + C_y)\,,$$
$$QFQ(\vec{k}, \kappa_x, \kappa_y) = \sum_{\vec{k}'=\vec{k}} QFQ(0, \kappa' x, \kappa' y)\,.$$

All other matrix elements can be found simply from symmetry considerations. The polarizability per ion is given according to Cowley's[40] general derivation

$$\alpha_\kappa = \frac{1}{v}\sum_{\kappa'} (DFD(\vec{k}=0))^{-1}_{\kappa x, \kappa' x}\,. \qquad \text{(A12)}$$

DFD is given by

$$DFD(\vec{k})_{\kappa x, \kappa' x'} = KD_\kappa\,\delta_{\kappa\kappa'}\,\delta_{xx'} + \lambda_K^D F(\vec{k}, \kappa x, \kappa' x')\lambda_{\kappa'}\,. \qquad \text{(A13)}$$

$(\lambda_\epsilon^D)^{-1}$ is formally the shell charge introduced by Cowley and Cochran.[30] The eigenvalue, eigenvector, and dynamical polarization depend only on the ratio between $(\lambda_\epsilon^Q)^2$ and KQ_ϵ, as one can easily derive from Eq. (6). It is, therefore, no approximation to assume that $\lambda_\epsilon^Q = \lambda_\epsilon^D$. In the SDM we have assumed that $KQ_\epsilon = KD_\epsilon$. The Axe model may be simply obtained by setting $\lambda^Q = 0$. The tensor of deformation is defined analogously to α.

*Work supported through a grant of the National Science Foundation.

†Work supported by the Deutsche Forschungsgemeinschaft.

‡Present address: Department of Chemistry, Purdue University, West Lafayette, Ind.

[1]M. Wagner and W. E. Bron, Phys. Rev. 139, A223 (1965).

[2]W. E. Bron and M. Wagner, Phys. Rev. 139, A233 (1965).

[3]W. E. Bron, Phys. Rev. 140, A2005 (1965).

[4]M. Wagner, Phys. Kondensierten Materie 4, 71 (1965).

[5]M. Wagner, Z. Physik 214, 1030 (1968).

[6]W. E. Bron, Phys. Rev. 185, 1163 (1969).

[7]D. Kühner and M. Wagner, Phys. Status Solidi 40, 517 (1970).

[8]D. Kühner, Z. Physik 230, 108 (1970).

[9]W. E. Bron, in *Physics of Impurity Centers in Crystals*, edited by K. Rebane (Estonian Academy of Sciences, USSR, 1971).

[10]D. Kühner, Ph. D. thesis (University of Stuttgart, 1970) (unpublished) (part of the thesis has appeared in Ref. 8).

[11]T. Timusk and M. Buchanan, Phys. Rev. 164, 345 (1967).

[12]M. Buchanan and E. J. Woll, Jr., Can. J. Phys. 47, 121 (1969).

[13]T. R. McGuire and M. W. Shafer, J. Appl. Phys. 35, 984 (1964); E. Catalano, R. G. Bedford, V. G. Silveira, and H. H. Wickman, J. Phys. Chem. Solids 30, 1613 (1969).

[14]Optovac, Inc., North Brookfield, Mass.

[15]D. L. Wood and W. Kaiser, Phys. Rev. 126, 2079 (1962).

[16]E. Cohen and H. J. Guggenheim, Phys. Rev. 175, 354 (1968).

[17]J. D. Axe and P. P. Sorokin, Phys. Rev. 130, 945 (1963).

[18]A. A. Maradudin, in *Solid State Physics*, edited by F. Seitz and D. Turnbull (Academic, New York, 1966), Vol. 19.

[19]P. P. Sorokin and W. V. Smith, *The Laser* (McGraw-Hill, New York, 1966).

[20]B. R. Judd, Phys. Rev. 127, 750 (1962).

[21]J. M. Lifshitz, Nuovo Cimento Suppl. 3, 716 (1956).

[22]M. V. Klein, Phys. Rev. 131, 1500 (1963).

[23](a) J. D. Axe, Phys. Rev. 139, A1215 (1965). (b) U. Schroeder, Solid State Commun. 4, 347 (1966); V. Nusslein and U. Schroeder, Phys. Status Solidi 21, 309 (1967).

[24]H. V. Lauer, Jr., K. A. Solberg, D. H. Kühner, and W. E. Bron, Phys. Letters 35, 219 (1971).

[25]K. Hisano, N. Ahama, and O. Matumura, J. Phys. Soc. Japan 20, 2294 (1965).

[26]R. P. Lowdes and D. H. Martin, Proc. Roy. Soc. (London) A308, 473 (1969).

[27]J. D. Axe and G. D. Pettit, J. Phys. Chem. Solids 27, 621 (1966).

[28]R. Srivastava, H. V. Lauer, Jr., L. L. Chase, and W. E. Bron, Phys. Letters 36A, 333 (1971).

[29]J. R. Tessman, A. H. Kahn, and W. Shockley, Phys. Rev. 92, 890 (1953).

[30]R. A. Cowley and W. Cochran, Phys. Rev. 131, 1030 (1963).

[31]E. W. Kellerman, Phil. Trans. Roy. Soc. London 238, 513 (1940).

[32]K. Stockar, Helv. Chim. Acta 33, 1409 (1950). We have assumed that the radius of Sm^{2+} equals that of Eu^{2+}.

[33]T. Timusk and R. W. Ward, Phys. Rev. Letters 22, 396 (1969).

[34]R. T. Harley, J. B. Page, Jr., and C. T. Walker, Phys. Rev. B 3, 1365 (1971).

[35](a) A. B. D. Woods, B. N. Brockhouse, R. A. Cowley, and W. Cochran, Phys. Rev. 131, 1025 (1963); G. J. S. Reid and T. Smith, Phys. Rev. B 1, 1833 (1970); G. Dolling, R. A. Cowley, C. Schiltenhelm, and I. M. Thorson, Phys. Rev. 14, F577 (1966); G. Dollius, H. G. Smith, R. M. Nicklow, P. R. Vijayaraghavan, and M. K. Wilkinson, *ibid.* 168, 970 (1967); J. R. D. Copley, R. W. Macpherson, and T. Timusk, *ibid.* 182, 965 (1969); G. Peehan, M. J. L. Sauter, and D. H. Saunderson, J. Phys. C 3, 1026 (1970). (b) S. Rolandson and G. Raunio, *ibid.* 4, 958 (1971).

[36]S. K. Sinha, Phys. Rev. 169, 477 (1968); 177, 1256 (1969); S. K. Sinha and R. P. Gupta, Phys. Rev. Letters 26, 1324 (1971).

[37]G. Leibfried and W. Ludwig, in *Solid State Physics*, edited by F. Seitz and D. Turnbull (Academic, New York,

1956), Vol. XII, p. 295.
[38]M. Born and K. Huang, *Dynamical Theory of Crystal Lattices* (Academic, New York, 1954).
[39]R. Srinivasan, Proc. Phys. Soc. (London) 72, 566 (1958).
[40]R. A. Cowley, Proc. Roy. Soc. (London) A268, 121 (1962).

PHYSICAL REVIEW B VOLUME 5, NUMBER 10 15 MAY 1972

Theory of Inelastic Scattering of Slow Electrons by Long-Wavelength Surface Optical Phonons*

E. Evans and D. L. Mills
Department of Physics, University of California, Irvine, California 92664
(Received 22 October 1971)

The purpose of this paper is to present a quantum-mechanical theory of the inelastic scattering of slow electrons by long-wavelength surface optical phonons for simple models of an ionic crystal and for a nonionic crystal such as silicon. It is argued that a quantum-mechanical approach is necessary for this problem. However, the expression we obtain for the one-phonon cross section is found to be identical to the one that follows from the earlier classical theory of Lucas and co-workers, provided one replaces their parameter P_0 by the quantum-mechanical reflection coefficient for specular reflection. The angular distribution of the scattered electrons and the energy dependence of the one-phonon cross section are discussed for the case of ZnO and silicon, where the surface optical modes have a very different character. For the surface mode in silicon, we define a dipole-moment effective charge, which is nonzero by virtue of the absence of inversion symmetry in the surface region. A quantitative estimate of the magnitude of this parameter is extracted from the data of Ibach.

I. INTRODUCTION

The effect of a surface on the phonon spectrum of crystals and on the magnetic properties of crystals has been the subject of a considerable theoretical effort. In many instances, the theory has reached a high level of sophistication, as one can see from the recent theoretical work of Chen *et al.*[1] on the lattice dynamics of ionic-crystal films.

However, while theoretical studies of the phonon and magnon spectrum of finite crystals indicate the presence of a complex variety of surface modes, and also important effects on the eigenvectors and frequency distribution of the bulk modes, until recently direct contact between detailed predictions of the theories and experimental data has been confined to the effect of the surface on quantities that depend on complicated averages over the phonon spectrum. Two examples are the effect of a surface on the phonon specific heat and the determination of the mean-square displacement in the surface from the temperature dependence of the low-energy-electron-diffraction (LEED) intensity.

The study of the energy-loss spectrum of slow electrons scattered from the surface should be, in principle, a powerful probe of the vibrational and magnetic properties of the surface region. However, such experiments are extremely difficult to carry out. If, for example, one wishes to study inelastic scattering of low-energy electrons by phonons utilizing low-energy electrons with energies in the range of 1 to 100 eV, then the incident beam must be extremely monoenergetic. It is very difficult in practice to obtain an electron beam sufficiently monochromatic to enable the study of the extremely small energy transfers involved in electron-phonon or electron-magnon scatterings.

However, Propst and Piper[2] have reported an experimental study of the vibrational modes of hydrogen and other species absorbed on the surface of tungsten by means of low-energy-electron spectroscopy. More recently, Ibach[3,4] has published two very complete experimental investigations of the inelastic scattering of low-energy electrons from the surfaces of ZnO and the (111) surface of silicon. In each case, a discrete-loss (and energy-gain) peak is observed in the energy spectrum of the emerging electrons. These loss and gain peaks are associated with emission and absorption of surface optical phonons by the electron.

In both ZnO and silicon, the scattering is apparently produced by a long-range electric field set up outside the crystal by the surface optical mode. That this is so is evident from the angular distribution of the inelastically scattered electrons.[3-5] In both cases it is observed that the inelastically